Check for updates

ADVANCED OPTICAL MATERIALS
www.advopticalmat.de

21951071, 2022, 22, Downloaded from https://onlinelibrary.wiley.com/doi/10.1002/adom.202201024 by Test, Wiley Online Library on [22/12/2022]. See the Terms and Conditions (https://onlinelibrary.wiley.com/terms-and-conditions) on Wiley Online Library for rules of use; OA articles are governed by the applicable Creative Commons License

Room Temperature Lasing in GeSn Microdisks Enabled by Strain Engineering

Dan Buca, Andjelika Bjelajac, Davide Spirito, Omar Concepción, Maksym Gromovyi, Emilie Sakat, Xavier Lafosse, Laurence Ferlazzo, Nils von den Driesch, Zoran Ikonic, Detlev Grützmacher, Giovanni Capellini, and Moustafa El Kurdi**

The success of GeSn alloys as active material for infrared lasers could pave the way toward a monolithic technology that can be manufactured within mainstream silicon photonics. Nonetheless, for operation on chip, lasing should occur at room temperature or beyond. Unfortunately, despite the intense research in recent years, many hurdles have yet to be overcome. An approach exploiting strain engineering to induce large tensile strain in micro-disk made of GeSn alloy with Sn content of 14 at% is presented here. This method enables robust multimode laser emission at room temperature. Furthermore, tensile strain enables proper valence band engineering; as a result, over a large range of operating temperatures, lower lasing thresholds are observed compared to high Sn content GeSn lasers operating at similar wavelength.

1. Introduction

Light emission in group IV materials is nowadays established through the use of GeSn semiconductor as optical active medium.[1,2] Lasing has already been observed for a large range of Sn contents[3–5] and different cavity configurations, such as micro-disks,[6] linear waveguides and photonic crystals,[7] and different heterostructure designs, for example, double heterostructure[8] and multi-quantum wells (MQW).[9] All these successes point to the great potential of GeSn as optical active medium, eventually enabling a monolithically integrated silicon photonic platform where all the technology-relevant devices, including the light sources, are manufactured using material and methods compatible with a state-of-the-art silicon foundry.

Along the path toward this goal, the scientific community has intensely worked on optimizing the laser performance, with the aim of bringing them to a level close to what is required by "real world" applications. The operating temperature can be increased toward room temperature by increasing the Sn content,[3] or using MQWs, similarly to the approach used for III–V lasers.[10] Furthermore, MQW structures are a safe way to decrease the laser threshold.[9]

The "directness," that is, the energy separation between Γ and L valleys of the conduction band (CB), $\Delta E_{L\Gamma} = E_L - E_\Gamma$,[3] increases with the Sn concentration, and the larger the directness the larger is the electron population in the Γ-valley, at a given temperature, and lower the electron inter-valley scattering between the Γ and L valleys. Indeed the lasing temperature, T_L was shown experimentally to increase from 80 K to 270 K once the Sn concentration is increased from 8 to 16 at% until recently.[4–6] Some of the main drawbacks of such relatively high Sn-content alloys, associated with the very challenging epitaxy are related to i) the large bulk/interface defects density, leading to enhanced non-radiative recombination; ii) the requirement of a graded GeSn buffer layer of large thicknesses to gradually relax the epitaxial compressive strain due to the lattice mismatch existing between the GeSn and the Ge/Si virtual substrate.[11,12]

Layer transfer technology provides several significant advantages to study the pathways to enhance the lasing performances of GeSn devices. One is the removal of the defective GeSn/Ge

D. Buca, O. Concepción, N. von den Driesch, D. Grützmacher
Institute of Semiconductor Nanoelectronics
Peter Grünberg Institute 9 (PGI 9) and JARA-Fundamentals of Future Information Technologies
Forschungszentrum Juelich
52428 Juelich, Germany
E-mail: d.m.buca@fz-juelich.de

A. Bjelajac, M. Gromovyi, E. Sakat, X. Lafosse, L. Ferlazzo, M. El Kurdi
CNRS
C2N
Université Paris-Saclay
10 boulevard Thomas Gobert, Palaiseau 91120, France
E-mail: moustafa.el-kurdi@u-psud.fr

D. Spirito, G. Capellini
IHP - Leibniz-Institut für innovative Mikroelektronik
Im Technologiepark 25, 15236 Frankfurt (Oder), Germany

Z. Ikonic
Pollard Institute
School of Electronic and Electrical Engineering
University of Leeds
Leeds LS2 9JT, UK

G. Capellini
Dipartimento di Scienze
Università Roma Tre
V.le G. Marconi 446, Rome I-00146, Italy

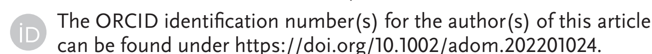
The ORCID identification number(s) for the author(s) of this article can be found under https://doi.org/10.1002/adom.202201024.

© 2022 The Authors. Advanced Optical Materials published by Wiley-VCH GmbH. This is an open access article under the terms of the Creative Commons Attribution-NonCommercial License, which permits use, distribution and reproduction in any medium, provided the original work is properly cited and is not used for commercial purposes.

DOI: 10.1002/adom.202201024

buffer interface, which reduces the carrier losses by non-radiative recombination, and consequently the laser threshold.[13–15] Another advantage arises from the GeSn layer transfer on an acceptor wafer containing a metallic interlayer. This plays the critical role of heat sink, dissipating the optical pumping induced heat. This technology, demonstrated in refs. [13, 15] applied to the GeSn layer with Sn content of ≈17% led to room temperature laser emission.[16,17]

Strain engineering, combined with layer transfer technology, is a proven path to improve the lasing performance, thus avoiding the need for excessive Sn content in the active layer.[13,18] Indeed, as presented in this study, by relying on strain engineering one can directly address both the maximum lasing temperature, by tuning the CB directness, and the laser threshold, due to a smaller density of states of the light hole (LH) valence band involved in the transition.

In this work, an "all-around" SiN stressor layer is used to induce tensile strain in a microdisk cavity featuring a moderately high GeSn content and by doing so, boost its lasing performance. In particular, this method enables robust multimode laser emission at room temperature. Moreover, we discuss how strain engineering can bring lasing threshold below those observed in higher Sn contents GeSn lasers, and how it makes this approach prospective in terms of high operation temperatures, while recent comprehensive advances have enabled electrically injected laser up to only 100 K.[19,20] We believe that the demonstration and comprehensive study of room temperature material gain under optical pumping, as performed in this work, should be useful for future achievement of robust and useable laser devices.

2. Results and Discussion

The band structure of a $Ge_{1-x}Sn_x$ alloy under different biaxial (epitaxial) strain conditions is shown in **Figure 1**. In the CB, the compressive biaxial strain ($\varepsilon < 0$) leads to a decrease of $\Delta E_{\Gamma L}$, equivalent to a reduced "effective Sn content." In the valence band (VB), the strain lifts the band degeneracy at $k = 0$, with

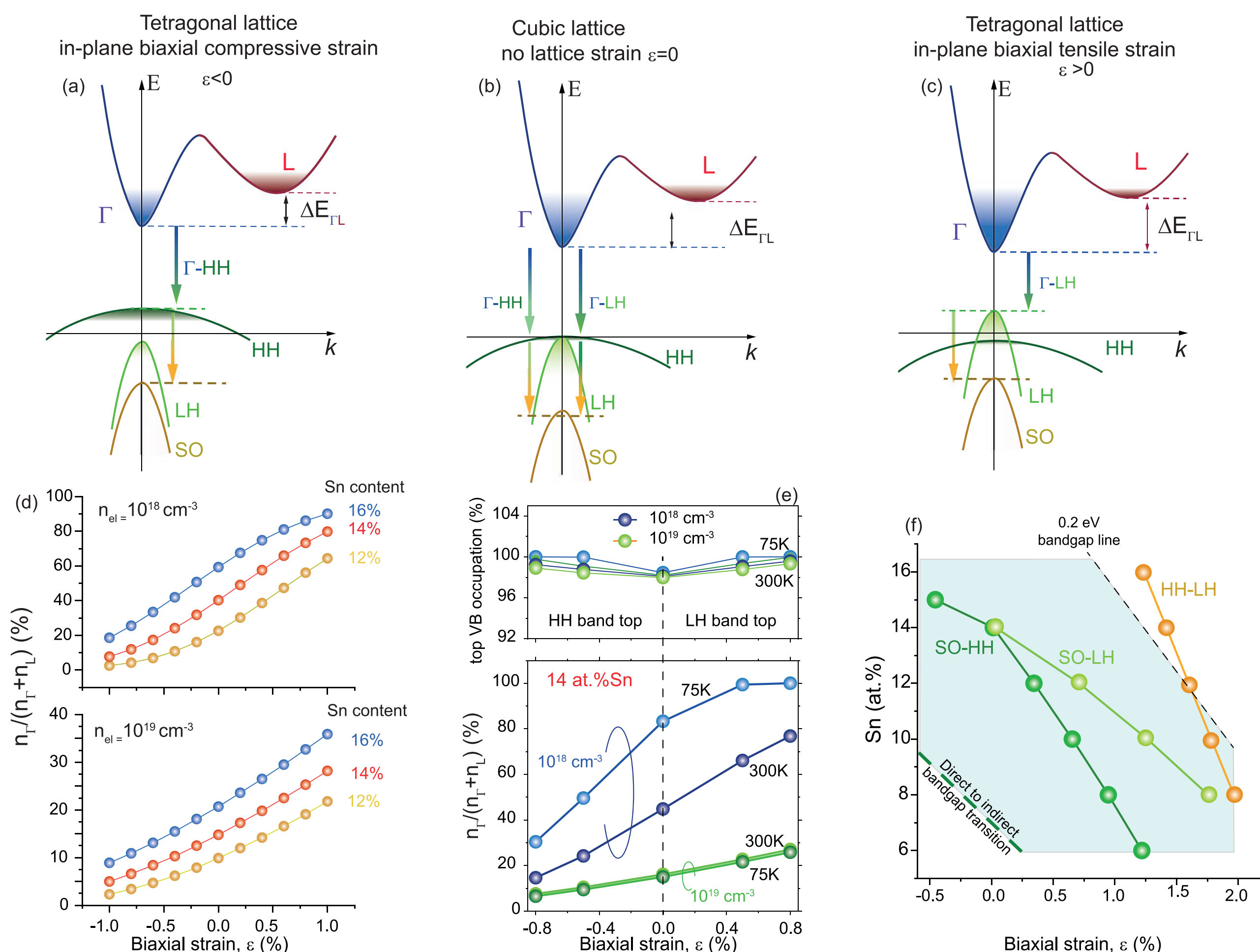

Figure 1. Electronic band structure at 300 K. a–c) Schematics of the strain dependent electronic band structure for direct bandgap GeSn alloys. From (a) to (c), there is an increase of the layer directness $\Delta E_{\Gamma L}$ and decrease of the band gap energy, and the position of the LH and HH bands is shifted from compressive to tensile strain. The main emission and the major re-absorption transitions are indicated by arrows. The steady state electron population at d) Γ-valley as a function of biaxial strain for various GeSn alloys at room temperature and e) T dependence for GeSn with 14 at% Sn. Both cases with total electron excess densities of 10^{18} and 10^{19} cm^{-3} are considered. f) The condition of equal energy between the inter-band emission with an IVB transition.

© 2022 The Authors. Advanced Optical Materials published by Wiley-VCH GmbH

21951071, 2022, 22, Downloaded from https://onlinelibrary.wiley.com/doi/10.1002/adom.202201024 by Test, Wiley Online Library on [22/12/2022]. See the Terms and Conditions (https://onlinelibrary.wiley.com/terms-and-conditions) on Wiley Online Library for rules of use; OA articles are governed by the applicable Creative Commons License

21951071, 2022, 22, Downloaded from https://onlinelibrary.wiley.com/doi/10.1002/adom.202201024 by Test, Wiley Online Library on [22/12/2022]. See the Terms and Conditions (https://onlinelibrary.wiley.com/terms-and-conditions) on Wiley Online Library for rules of use; OA articles are governed by the applicable Creative Commons License

the heavy hole (HH) band shifting to higher energy. The radiative recombination, that is, the laser transition, then takes place between the Γ-valley and the HH-band (Figure 1a) and its energy increases with the compressive strain value. Conversely, a tensile biaxial strain ($\varepsilon > 0$) promotes the "directness" and decreases the bandgap energy, pushing the light emission deeper in the IR range. Furthermore, the tensile strain shifts the LH band up, above the HH band and, consequently, the inter-band radiative recombination occurs between Γ-valley and the LH band (Figure 1c). At zero strain, that is, cubic crystal structure, both Γ-valley to LH and HH bands transitions are possible and the directness is determined only by the Sn content (Figure 1b).

The electron population in the Γ CB depends not only on the Γ-L energy spacing $\Delta E_{\Gamma L}$ through the Sn composition and strain, but also on the total number of electrons in the CB and on the temperature (Figure 1d,e). A higher number of electron or temperature leads to increased electron fraction in the indirect L-band, which has a larger density of states (DOS). As a consequence, the fraction of electrons populating the Γ valley is reduced, with detrimental effect on gain. Tensile strain is a key element to reduce the laser threshold and increase the maximum lasing temperature. In the valence band most of the carriers (>95%) are occupying the upper valence band (VB) as depicted in Figure 1e.

The different VB splitting obtained for different signs of strain has a paramount importance in the gain optimization, through: i) the different DOS of LH and HH bands; ii) the different strengths of the intra-valence band (IVB) transitions; iii) the absorption losses, that is, affecting the energy where the emitted photons re-absorption can occur, based on LH-HH, LH-split-off (SO) band or HH-SO transitions. Figure 1f shows the (Sn at%, ε) values for which the laser transition energy equals one of the IVB transition energies, and, therefore, re-absorption proportional to the transition strength, occurs, with a consequent decrease of the net optical gain. The region of high interest for lasing under tensile strain at room temperature is where (Sn at%, ε) values are beyond those of "direct–indirect transition" line, given by the values where the GeSn becomes a direct bandgap semiconductor (green dotted line), and the MIR upper limit, set here at 0.2 eV (≈6 µm).

In case of compressive strain, the Γ–HH radiative transition occurs typically at a much larger energy than the IVB transitions energies for Sn composition up to 12 at% (not shown here). In contrast, the energy of the Γ–LH transition under tensile strain equals the IVB transition energy at lower Sn contents, becoming even smaller for high strain.

Based on the above discussion, a $Ge_{0.86}Sn_{0.14}$ layer has been chosen as laser active medium, manufactured as layer-transferred µ-disks, as schematically described in **Figure 2**a,b, following the procedure we have first described in ref. [13].

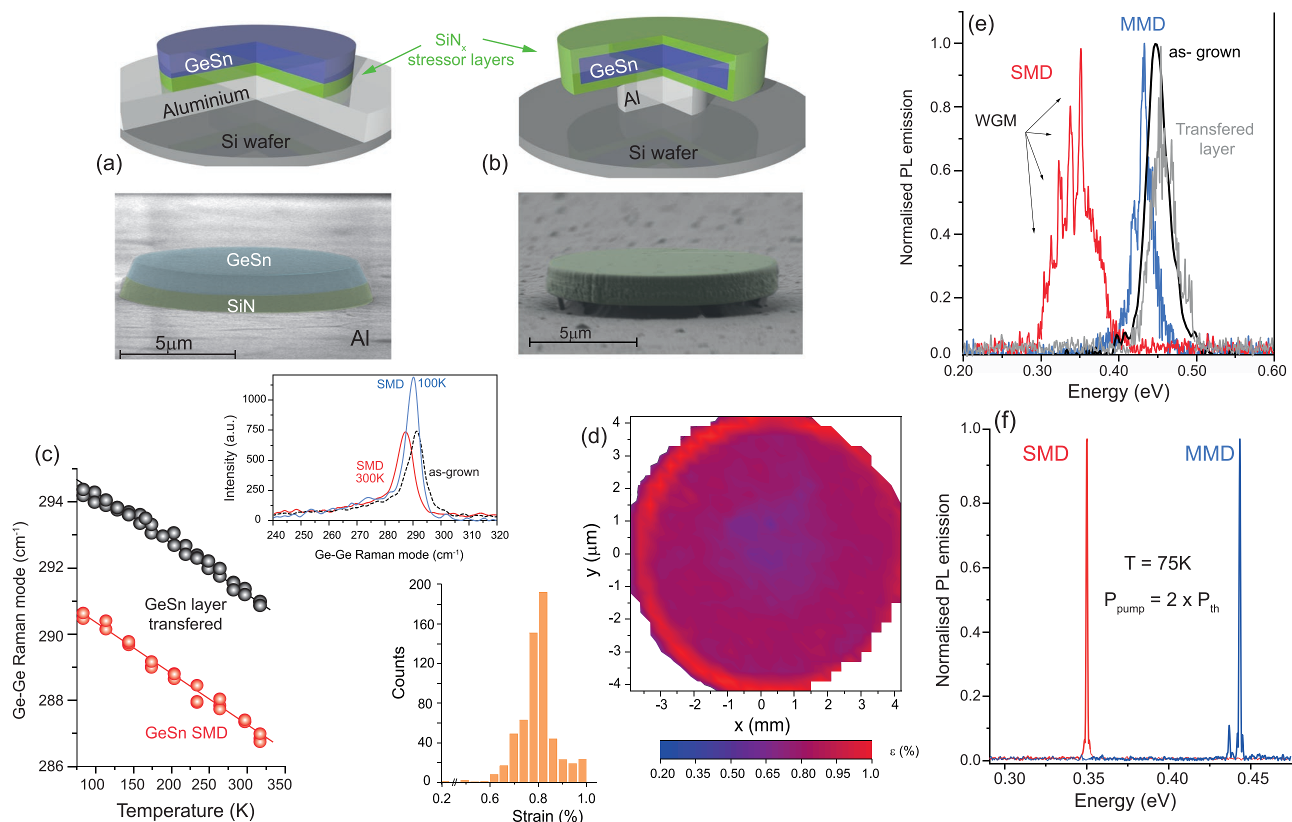

Figure 2. Material characterization. a,b) Skatches and SEM images of MMD and SMD lasers. c) Temperature dependent Ge–Ge Raman backscattered resonance under 532 nm wavelength excitation. Inset: Raman spectra of the as-grown and SMD at 100 K and 300 K. d) Strain mapping from 2D Raman analysis of a SMD of 8 µm diameter. Inset: Histogram indicating a tensile strain of 0.8% in the disk and 1% in the under-etched disk area. e) Photoluminescence spectra from SMD and MMD of 9 µm diameter as compared to PL spectra of transferred layer and as-grown layer. f) Laser emission spectra from SMD and MMD measured under pulsed excitation power of twice the lasing threshold.

© 2022 The Authors. Advanced Optical Materials published by Wiley-VCH GmbH

The investigated $Ge_{0.86}Sn_{0.14}$ active layers were epitaxially grown on thick Ge/Si(001) 200 mm virtual substrate by means of an industry-grade chemical vapor deposition reactor, using commercially-available digermane (Ge_2H_6) and tin-tetrachloride ($SnCl_4$) precursors. Details on the growth process can be found elsewhere.[20,21]

The grown layer was transferred so that the two structures, the nearly relaxed and the strained one, can be compared while both taking advantage of interface defects removal, as shown in refs. [13, 15]. Before the layer transfer, a SiN stressor layer followed by Al layer was deposited on the top surface of the GeSn. The SiN layer above the Al layer, below the GeSn layer, thus came from deposition prior to the layer transfer.

The transferred layer structure is then processed into mesa GeSn micro-disks (called "MMD") by etching the GeSn and SiN layers down to the buried Al layer (Figure 2a). In the second step the GeSn free-standing rims of the microdisks were formed by selective under-etching the Al base layer. A second SiN stressor layer is then deposited on the structure forming an "all-around stressor design,"[20] Figure 2b, which increases and homogenizes the tensile strain, as seen in Figure 2d. Note that the SiN layer has a large compressive built-in strain that can relax after the layer is patterned, such that tensile strain is released only for patterned transferred layers. This strained microdisk is further called "SMD."

2.1. Material Characterization

Temperature dependent micro-Raman spectroscopy in back-scattering geometry was performed to determine the strain evolution (Figure 2c) and spatial distribution in the GeSn microdisks (Figure 2d). Measurements were conducted using an optical excitation at $\lambda = 532$ nm and a 100× NA = 0.65 at a non-heating incident power density $P_0 = 25$ kW cm^{-2}, for an estimated lateral resolution of 450 nm.[22] In the inset of Figure 2c the Raman spectral region corresponding to the Ge-Ge mode is shown. The biaxial strain in the structures was calculated using a strain-Raman shift coefficient $b = -550 \pm 25$ cm^{-1}, as obtained by direct comparison with strain measurements performed by reciprocal space X-ray diffraction acquired on the same sample, following the procedure described in ref. [23]. The Raman map in Figure 2d, evidences a uniform strain distribution in the SMD sample centered at a tensile strain value of $\varepsilon = 0.8\%$, with a slightly increased strain of $\varepsilon \approx 1\%$ at the disk periphery (see histogram inset in Figure 2d). As evidenced in Figure 2c, the Raman modes in unpatterned GeSn layer and on the SMD evolve in parallel, indicating that no additional strain is generated during temperature change. This reinforces the interest for our all-around stressor method to apply constant tensile strain with temperature. This is different from the case of suspended GeSn on Ge microbridges as proposed in ref. [5] where the tensile strain strongly changes with temperature.

The strain evaluated by Raman spectroscopy is in agreement with that derived by analyzing photoluminescence (PL) spectra of the GeSn layer for the case of transferred only, MMD, and SMD samples as shown in Figure 2e. The PL spectra are taken under non-lasing continuous-wave (cw) optical pumping conditions. Whispering gallery modes (WGM) are clearly observed in both the MMD and SMD samples. The PL of the as-grown layer is also plotted for comparison. Upon comparing the PL spectra with the theoretically calculated electronic band structure, it can be concluded that the mesa patterning leads to a strain free GeSn/SiN/Al stack. The under-etching of the Al post followed by second SiN stressor coverage, leading to SiN/GeSn/SiN strained disk,[24] red-shifts the PL emission by ≈95 meV, as expected for a GeSn layer under a biaxial tensile strain $\varepsilon \approx +0.8\%$.

Next, the laser emission of the two MMD and SMD structures is presented. Differently the previously reported experiments in the literature, where similar analyses were performed but on different GeSn content layers, different processing, and, more importantly, on samples with different amounts of strain, here samples made from exactly the same GeSn grown wafer, processed simultaneously, and analyzed under the same experimental conditions are compared. Lasing experiments were performed using a µ-PL setup with 1550 nm wavelength under 2 ns pulsed excitation with repetition rate of 400 kHz. Note that the surface reflectivities of the samples with and without the SiN are very similar, around 35–37%. The absorption length of the 1550 nm pump in GeSn is expected to be of the order of 50 nm, much thinner than the GeSn layer thickness. Therefore, it can be assumed that the total absorbed optical power from the incident pump is equivalent to 65% for both sample MMDs and SMDs. This absorbed power is the most representative value for determining the correct laser threshold values. However, while these data are later benchmarked against the literature data where the incident power is given, the correction factor due to reflectivity is not accounted for.

At 75 K both mesa and strained MDs cavities show clear and robust lasing at energies of 0.44 eV ($\lambda = 2.82$ µm) and 0.35 eV ($\lambda = 3.5$ µm), respectively. The spectra in Figure 2f are taken at optical pump densities twice the laser threshold of 20 and 12 kW cm^{-2} for the MMD and SMD, respectively, and show laser emission, and negligible spontaneous emission background. The laser emission clearly shows a red shift of 95 meV for the case of SMD with respect to the MMD, similarly to the spectral red shift observed for PL spectra of Figure 2d. The investigated cavities have similar diameter of 9 µm that supports a large density of whispering gallery modes in the 3–4 µm wavelength range.

Detailed lasing characteristics of the MMD structure are shown in **Figure 3**. Even at low power densities multimode lasing is already present, indicating a relatively high and large broad spectral gain. The largely multimode emission, up to the laser quenching temperature, is better exemplified by the spectra in Figure 3a taken under a pump density of 200 kW cm^{-2} at temperature between 75 K and the maximum lasing temperature of 265 K. At the highest operating T_L = 265 K the multimode emission is observed by increasing the pumping power density to 500 kW cm^{-2}, as shown in Figure 3b, with a main laser mode peaked at an energy of 0.395 eV (λ = 3.14 µm). However, at such high power and high temperature the lasing optical modes appear on top of a spontaneous emission background, indicating inefficient carrier dynamics, as highlighted in Figure 3c, where the spectra at 75 K and 265 K are displayed for direct comparison. The typical light-in–light-out (L–L) laser characteristic offers additional information on

© 2022 The Authors. Advanced Optical Materials published by Wiley-VCH GmbH
21951071, 2022, 22, Downloaded from https://onlinelibrary.wiley.com/doi/10.1002/adom.202201024 by Test, Wiley Online Library on [22/12/2022]. See the Terms and Conditions (https://onlinelibrary.wiley.com/terms-and-conditions) on Wiley Online Library for rules of use; OA articles are governed by the applicable Creative Commons License

21951071, 2022, 22, Downloaded from https://onlinelibrary.wiley.com/doi/10.1002/adom.202201024 by Test, Wiley Online Library on [22/12/2022]. See the Terms and Conditions (https://onlinelibrary.wiley.com/terms-and-conditions) on Wiley Online Library for rules of use; OA articles are governed by the applicable Creative Commons License

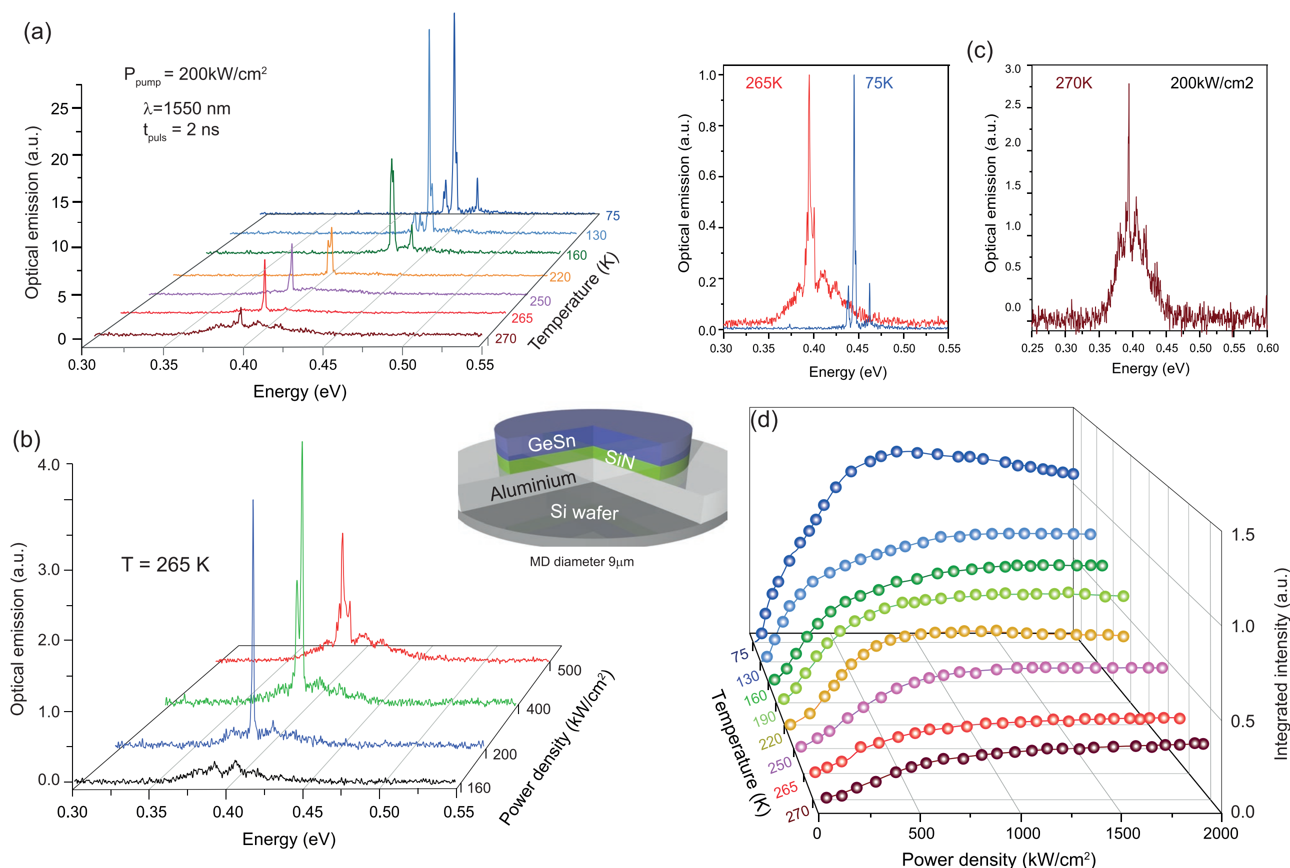

Figure 3. Strain relaxed microdisks. Laser properties of relaxed 9 µm diameter GeSn mesa micro-disks MMD. a) Temperature dependence of the PL emission under 200 kW cm^{-2} optical pumping. b) Power dependence of the PL spectra at 265 K. c) Laser spectra for 200 kW cm^{-2} optical pumping at 75, 265, and 270 K. d) Temperature dependent L–L characteristic. Very weak roll-off is seen with increasing pumping power.

the laser emission. An "S-shape" form with clear gain saturation after exponential intensity increase is seen at all temperatures. The use of the buried Al layer efficiently drags away the pumping-induced heat[25] and a small emission roll-off appears at very high pump densities, larger than 1 MW cm^{-2}. At 270 K the L–L characteristic is linear, with spectra showing a sharp emission at the same energy as the laser at 265 K. Since this mode does not change with the pumping density and, considering the large luminescence background, it is attributed to PL-WGM and not to laser emission. The maximal temperature of laser operation is thus reasonably considered as 265 K, which is much higher than that reported for equivalent Sn composition in the literature.[26–28] The main reason here for improved T_L resides in the advantages of the layer transfer strategy as discussed in ref. [15] like the removal of interface defects.[16,17]

As discussed in the introduction the tensile strain promotes the CB directness and shifts the laser transition from Γ- HH to Γ-LH. As discussed above this is expected to reduce the carrier density at threshold. Indeed, at low temperature this effect is clearly seen, as the SMD laser threshold value (12 kW cm^{-2} at 75 K; **Figure 4**a), is approximately half that of the MMD. The robustness of laser is witnessed by the normalized laser spectra at 75 K under extremely high pumping power density (1 MW cm^{-2}, Figure 4b) which presents a distribution of laser modes spreading over an energy range of ≈80 meV. This indicates a very high optical gain over a broad spectral range in the SMD, that is preserved even at room temperature, as shown in Figure 4c,d, where laser emission at an energy of 0.34 eV (λ = 3.64 µm) is observed. Here, the laser threshold is ≈550 kW cm^{-2}. The high temperature LL- characteristics of SMD are presented in Figure 4e. Here, the laser threshold is ≈550 kW cm^{-2} at 300 K, while no laser threshold, both in the emission spectra (Figure 4c) and LL characteristics (Figure 4e), was observed at temperatures of 305 K and above. As can be observed, in the inset of Figure 4e the lasing peak linewidth extracted from emission spectra at 300 K (shown in Figure 4d) reduces by almost a factor of two, from 1.5 meV below threshold under 500 kW cm^{-2} pump power to 0.8 meV above the threshold at 600 kW cm^{-2} pump power. This feature is a clear signature of laser transition, with the emission regime changing from incoherent to coherent, as proposed by Schawlow–Townes theory.[13,16] Interestingly the LL-characteristics show a roll-off effect for power densities in excess of 600 kW cm^{-2}, a value approximately half of that measured in the case of the MMD samples (Figure 3e). This is attributed to the partial etching of the Al pedestal in SMD case (Figure 2) which reduces the pump-induced heat transport efficiency. Indeed, GeSn alloys thermal conductivity strongly decreases with increasing the Sn content, reaching ≈4 W (cm K)$^{-1}$ for 14 at% Sn.[22]

© 2022 The Authors. Advanced Optical Materials published by Wiley-VCH GmbH

ADVANCED OPTICAL MATERIALS
www.advopticalmat.de

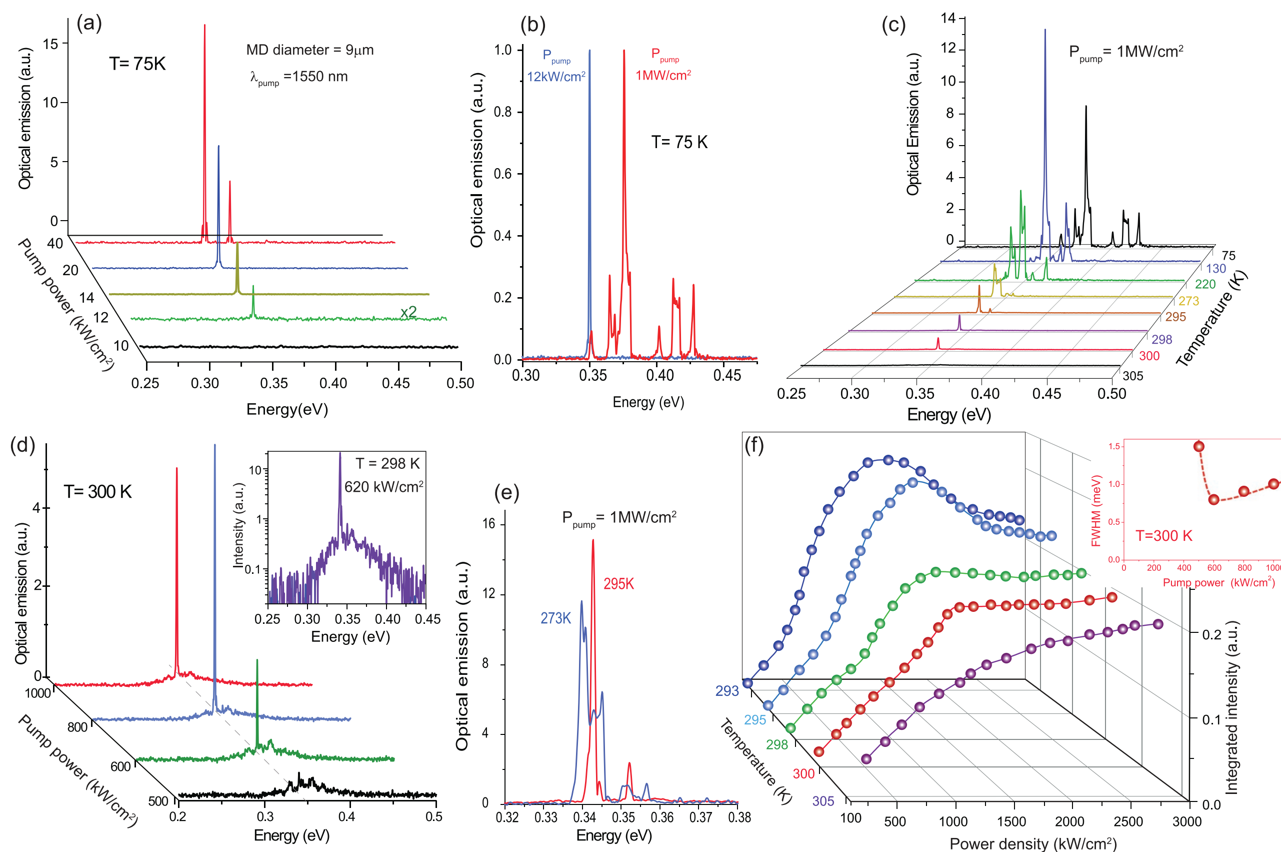

Figure 4. Tensile strain microdisks. Laser properties of 1% tensile strained 9 µm diameter GeSn micro-disk. a) Power dependence of the PL spectra at 75 K. b) Laser spectra under 12 and 1000 kW cm^{-2} optical pumping at 75 K indicating broad energy gain. c) Temperature dependence of the PL emission under 1000 kW cm^{-2} optical pumping. d) Power dependence of the PL spectra at 300 K. Inset: 298 K spectrum in log scale. e) Laser spectra comparison at 273 K and 298 K under 1 MW cm^{-2} pumping showing large gain over broad energy range. f) Temperature dependent L–L characteristic. Roll-off is seen with increasing pumping power. The inset shows the lasing mode linewidth (full width at half maximum) as a function of the pump power that was extracted from emission spectra in (d) at 300 K. We observe a clear linewidth reduction by a factor of around two at threshold.

The temperature dependent laser threshold for both MMD and SMD lasers is presented in **Figure 5**a. The results can be directly compared with very recent literature data for GeSn layers with concentrations of 16.9 at% Sn[17] and 17.2 at% Sn.[16] Strikingly, while lasing at 300 K is achieved in these cases, the laser thresholds are significantly higher at all temperatures

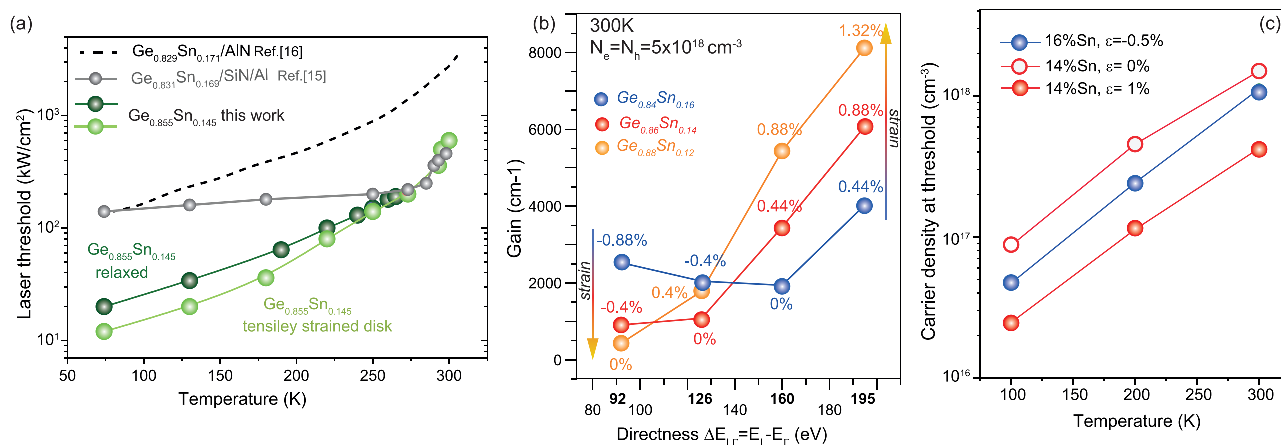

Figure 5. Laser threshold and modeling. a) Room temperature laser threshold benchmark. The power density represents the incident pump power as discussed above. The absorbed laser power is $P_{abs} = 0.65 \cdot P_{incident}$. b) Comparison of the net-gain at 300 K and same directness, for GeSn lasers with 12, 14, and 16 at% Sn content. The directness is obtained at different strain levels, as indicated in the graph (c). Carrier density at threshold for GeSn lasers with 14 and 16 at% Sn content under different biaxial lattice strains.

© 2022 The Authors. Advanced Optical Materials published by Wiley-VCH GmbH

21951071, 2022, 22, Downloaded from https://onlinelibrary.wiley.com/doi/10.1002/adom.202201024 by Test, Wiley Online Library on [22/12/2022]. See the Terms and Conditions (https://onlinelibrary.wiley.com/terms-and-conditions) on Wiley Online Library for rules of use; OA articles are governed by the applicable Creative Commons License

for 17.2 at% Sn layer[17] and at temperatures below 250 K for 16.9 at%Sn[16] than those measured for both structures here. Also intriguing is the difference in the laser emission, that is single-mode in ref. [17] while it is definitely multimode here.

Another direct literature comparison is the ref. [16] employing a relaxed $Ge_{0.831}Sn_{0.169}$ laser structure that was fabricated using the same processing as for the present MMD. Both structures relax the residual as-grown compressive strain after layer transfer, but the Sn-content is however near 17 at%Sn in ref. [16] while it is 14 at%Sn here. From Figure 5a the low temperature threshold is larger for higher Sn-content layer, while modeling predicts a similar carrier density at thresholds. This may be related to a larger point defects density for larger Sn-content GeSn alloys which is not accounted for in the gain modeling.

The role of the strain on the net gain, g, highlighted in Figure 5b, was modeled for GeSn active layers with Sn contents of 12, 14, and 16 at% under different strain conditions, as presented in Figure 5b. The present gain modeling accounted for the IVBA losses that can be tuned both by Sn-content and by tensile strain, as discussed in Figure 1. For a fair comparison, the strain is chosen so that the three materials have the same directness $\Delta E_{L\Gamma}$. When the strain is only compressive or zero, for example, $\Delta E_{L\Gamma} = 92$ meV for $\varepsilon_{12\%} = 0\%$, $\varepsilon_{14\%} = -0.44\%$, $\varepsilon_{16\%} = -0.88\%$, the maximum net gain occurs for larger Sn content: $g_{12\%Sn} < g_{14\%Sn} < g_{16\%Sn}$. When the strain is only tensile or zero, for example, $\Delta E_{L\Gamma} = 165$ meV for $\varepsilon_{12\%} = 0.88\%$, $\varepsilon_{14\%} = 0.44\%$, $\varepsilon_{16\%} = 0\%$, the maximum gain is obtained in the alloy with the lowest Sn content, $g_{12\%Sn} > g_{14\%Sn} > g_{16\%Sn}$.

By comparing these cases, it can be concluded that the strain is the parameter that has a larger impact on gain than the alloy composition. The larger the strain, the larger is the splitting of HH and LH bands, so more holes will populate the higher one of them, and produce a larger gain for the corresponding polarization (x,y for HH, and z for LH).

If some alloys are compressive strained and others are tensile strained to reach the same directness, as is the case for $\Delta E_{L\Gamma} = 126$ meV in Figure 5b, the largest gain does not have to be in the alloy with the lowest Sn content.

As already stated, one of the advantages of tensile strain is to promote radiative transitions toward lower density of states LH band, which reduces the carrier density required for transparency, hence reducing the lasing threshold, as shown in Figure 5a,c. The carrier density at threshold (zero net gain) at all temperatures is lower for the strained $Ge_{0.86}Sn_{0.14}$ layer than in relaxed or slightly compressively strained $Ge_{0.84}Sn_{0.16}$ layers.

The advantage of higher Sn content is, however, best seen if the strain in all alloys is zero, where the largest gain occurs in the alloy with the largest at% Sn, that is, $Ge_{0.84}Sn_{0.16}$ alloy. This is reflected in the higher lasing temperature of 300 K for the relaxed $Ge_{0.831}Sn_{0.169}$ layer[16] compared to 265 K for the relaxed $Ge_{0.86}Sn_{0.14}$ mesa MD case. Finally, introducing tensile strain to increase $\Delta E_{L\Gamma}$ raises the lasing temperature of $Ge_{0.86}Sn_{0.14}$ to 300 K. This again underlines the expected performance improvement offered by a larger energy difference between the Γ- and L- valley CBs.

We can now briefly summarize the physical background of the increase of gain, at fixed carrier injection, thanks to applied tensile strain. This is first due to the fact that c.b.-HH and c.b.-LH transitions give gain predominantly for x- or z-polarization, so the density of the increased holes in one of valence bands (due to their splitting, and with equilibrium distribution of holes between them) gives larger gain for one polarization, that can then preferentially amplify a given cavity polarized mode, compared to the case of no splitting where both polarizations have equal gain. Therefore, the threshold for transparency is reached for lower injected carrier density thanks to HH–LH separation.

Second, the transparency is reached when the Fermi level positions in the CB (E_{FC}) and the valence band (E_{FV}) are such that the energy separation E_{FC}-E_{FV} exceeds the band gap energy. One can thus reach transparency faster (i.e., get a faster increase of E_{FC} and/or decrease of E_{FV} with increasing carrier injection) by reducing the valence band DOS, or the CB DOS, or both. In any case, the reduction of one of the VB or CB DOS is sufficient to reduce threshold for transparency (and in this system it indeed takes place for VB DOS only). All these arguments are of course verified by rigorous modeling of gain for different strain/Sn content conditions.

The above gain modeling, to find its dependence on Sn and lattice strain, gives a good insight in the lasing dynamics, explains the experimental benchmarked data, and shows the direction to follow for designing an efficient room temperature laser. However, it does not explain the limited 300 K lasing temperature, nor almost the same laser thresholds for strained $Ge_{0.86}Sn_{0.14}$ and relaxed $Ge_{0.831}Sn_{0.169}$ layers at higher temperatures.

However, the presented data and modeling do not indicate a limited, 300 K lasing temperature, and also cannot explain the same laser thresholds for strained $Ge_{0.86}Sn_{0.14}$ and relaxed $Ge_{0.831}Sn_{0.169}$ layers at ≈300 K. As mentioned above, high thresholds can be attributed to the large point defects density in high Sn content alloys that has been evidenced experimentally in several works.[29] Further investigation, which accounts for surface passivation, should also be helpful to mitigate the influence of surface trap activation with temperature in carrier recombination dynamics.[30] Such defect densities and surface recombination are not taken into account in the above modeling and should be considered as important issues to overcome in view of reduction of the laser thresholds,[14] and continuous wave operation at room temperature.[13] Further strategies, combining quantum confinement of carriers and strain engineering of the band structure, should have a high potential to overcome point defects and surface recombination losses, and to reach the room temperature lasing with significantly reduced thresholds.[18,31,32]

3. Conclusion

The role and the advantages of tensile strain in band structure engineering and optical gain of GeSn alloys for improved laser thresholds and operation temperatures were discussed and experimentally implemented. The used all-around SiN stressor technology is based on layer transfer strategy that allowed for inducing of a state of the art ≈1% tensile strain into a GeSn layer with 14 at% of Sn. The clear benefit of tensile strain is proved via the lasing characteristics of microdisk cavities

© 2022 The Authors. Advanced Optical Materials published by Wiley-VCH GmbH

21951071, 2022, 22, Downloaded from https://onlinelibrary.wiley.com/doi/10.1002/adom.202201024 by Test, Wiley Online Library on [22/12/2022]. See the Terms and Conditions (https://onlinelibrary.wiley.com/terms-and-conditions) on Wiley Online Library for rules of use; OA articles are governed by the applicable Creative Commons License

with/out all-around SiN stressors. The tensile strain offers a robustness of laser emission up to 300 K, compared to 265 K for unstrained microdisk. Lasing thresholds were found significantly lower for tensile strained structures. Increasing the Sn-content up to a challenging value of 17% was the only way admitted by mainstream research to reach room temperature lasing in GeSn. In the future, tensile strain engineering should thus be considered as a key ingredient to mitigate the limitations encountered when using only the Sn content to optimize optical gain.

Acknowledgements

The authors thank the German Research Foundation (DFG) under project "SiGeSn lasers for Si photonic" and German Federal Ministry of Education and Research (BMBF) under "ForMikro-SiGeSn NanoFETs" for partial financial support. This work was also supported by the French RENATECH network, the French National Research Agency (Agence Nationale de la Recherche, ANR) through funding of the ELEGANTE project (ANR-17-CE24-0015). A.B. was supported by Nano2022 IPCEI project with STMicroelectronics.

Conflict of Interest

The authors declare no conflict of interest.

Data Availability Statement

The data that support the findings of this study are available from the corresponding author upon reasonable request.

Keywords

GeSn band structure, GeSnOI, mid-infrared laser, room temperature GeSn laser, strain engineering

Received: May 4, 2022
Revised: July 2, 2022
Published online: August 21, 2022

[1] R. A. Soref, D. Buca, S.-Q. Yu, *Opt. Photonics News* **2016**, *27*, 32.
[2] O. Moutanabbir, S. Assali, X. Gong, E. O'Reilly, C. A. Broderick, B. Marzban, J. Witzens, W. Du, S.-Q. Yu, A. Chelnokov, D. Buca, D. Nam, *Appl. Phys. Lett.* **2021**, *118*, 110502.
[3] S. Wirths, R. Geiger, N. von den Driesch, G. Mussler, T. Stoica, S. Mantl, Z. Ikonic, M. Luysberg, S. Chiussi, J. M. Hartmann, H. Sigg, J. Faist, D. Buca, D. Grützmacher, *Nat. Photonics* **2015**, *9*, 88.
[4] Y. Zhou, W. Dou, W. Du, S. Ojo, H. Tran, S. A. Ghetmiri, J. Liu, G. Sun, R. Soref, J. Margetis, J. Tolle, B. Li, Z. Chen, M. Mortazavi, S. Q. Yu, *ACS Photonics* **2019**, *6*, 1434.
[5] J. Chrétien, N. Pauc, F. Armand Pilon, M. Bertrand, Q. M. Thai, L. Casiez, N. Bernier, H. Dansas, P. Gergaud, E. Delamadeleine, R. Khazaka, H. Sigg, J. Faist, A. Chelnokov, V. Reboud, J. M. Hartmann, V. Calvo, *ACS Photonics* **2019**, *6*, 2462.
[6] D. Stange, S. Wirths, R. Geiger, C. Schulte-Braucks, B. Marzban, N. V. D. Driesch, G. Mussler, T. Zabel, T. Stoica, J.-M. Hartmann, S. Mantl, Z. Ikonic, D. Grützmacher, H. Sigg, J. Witzens, D. Buca, *ACS Photonics* **2016**, *3*, 1279.
[7] Q. M. Thai, N. Pauc, J. Aubin, M. Bertrand, J. Chrétien, A. Chelnokov, J. M. Hartmann, V. Reboud, V. Calvo, *Appl. Phys. Lett.* **2018**, *113*, 051104.
[8] N. von den Driesch, D. Stange, D. Rainko, I. Povstugar, P. Zaumseil, G. Capellini, T. Schröder, T. Denneulin, Z. Ikonic, J.-M. Hartmann, H. Sigg, S. Mantl, D. Grützmacher, D. Buca, *Adv. Sci.* **2018**, *5*, 1700955.
[9] D. Stange, N. Von Den Driesch, T. Zabel, F. Armand-Pilon, D. Rainko, B. Marzban, P. Zaumseil, J. M. Hartmann, Z. Ikonic, G. Capellini, S. Mantl, H. Sigg, J. Witzens, D. Grützmacher, D. Buca, *ACS Photonics* **2018**, *5*, 4628.
[10] C. Weisbuch, J. Nagle, *Phys. Scr.* **1987**, *1987*, 209.
[11] J. Margetis, A. Mosleh, S. Al-Kabi, S. A. Ghetmiri, W. Du, W. Dou, M. Benamara, B. Li, M. Mortazavi, H. A. Naseem, S. Q. Yu, J. Tolle, *J. Cryst. Growth* **2017**, *463*, 128.
[12] S. Al-Kabi, S. A. Ghetmiri, J. Margetis, T. Pham, Y. Zhou, W. Dou, B. Collier, R. Quinde, W. Du, A. Mosleh, J. Liu, G. Sun, R. A. Soref, J. Tolle, B. Li, M. Mortazavi, H. A. Naseem, S. Yu, *Appl. Phys. Lett.* **2016**, *109*, 171105.
[13] A. Elbaz, D. Buca, N. von den Driesch, K. Pantzas, G. Patriarche, N. Zerounian, E. Herth, X. Checoury, S. Sauvage, I. Sagnes, A. Foti, R. Ossikovski, J. M. Hartmann, F. Boeuf, Z. Ikonic, P. Boucaud, D. Grützmacher, M. El Kurdi, *Nat. Photonics* **2020**, *14*, 375.
[14] A. Elbaz, R. Arefin, E. Sakat, B. Wang, E. Herth, G. Patriarche, A. Foti, R. Ossikovski, S. Sauvage, X. Checoury, K. Pantzas, I. Sagnes, J. Chrétien, L. Casiez, M. Bertrand, V. Calvo, N. Pauc, A. Chelnokov, P. Boucaud, F. Boeuf, V. Reboud, J.-M. Hartmann, M. El Kurdi, *ACS Photonics* **2020**, *7*, 2713.
[15] B. Wang, E. Sakat, E. Herth, M. Gromovyi, A. Bjelajac, J. Chaste, G. Patriarche, P. Boucaud, F. Boeuf, N. Pauc, V. Calvo, J. Chrétien, M. Frauenrath, A. Chelnokov, V. Reboud, J. M. Hartmann, M. El Kurdi, *Light: Sci. Appl.* **2021**, *10*, 232.
[16] A. Bjelajac, M. Gromovyi, E. Sakat, B. Wang, G. Patriarche, N. Pauc, V. Calvo, P. Boucaud, F. Boeuf, A. Chelnokov, V. Reboud, M. Frauenrath, J.-M. Hartmann, M. El Kurdi, *Opt. Express* **2022**, *30*, 3954.
[17] J. Chrétien, Q. M. Thai, M. Frauenrath, L. Casiez, A. Chelnokov, V. Reboud, J. M. Hartmann, M. El Kurdi, N. Pauc, V. Calvo, *Appl. Phys. Lett.* **2022**, *120*, 051107.
[18] D. Rainko, Z. Ikonic, A. Elbaz, N. von den Driesch, D. Stange, E. Herth, P. Boucaud, M. El Kurdi, D. Grützmacher, D. Buca, *Sci. Rep.* **2019**, *9*, 259.
[19] Y. Zhou, Y. Miao, S. Ojo, H. Tran, G. Abernathy, J. M. Grant, S. Amoah, G. Salamo, W. Du, J. Liu, J. Margetis, J. Tolle, Y. Zhang, G. Sun, R. A. Soref, B. Li, S.-Q. Yu, *Optica* **2020**, *7*, 924.
[20] Y. Zhou, S. Ojo, C.-W. Wu, Y. Miao, H. Tran, J. M. Grant, G. Abernathy, S. Amoah, J. Bass, G. Salamo, W. Du, G.-E. Chang, J. Liu, J. Margetis, J. Tolle, Y.-H. Zhang, G. Sun, R. A. Soref, B. Li, S.-Q. Yu, *Photonics Res.* **2022**, *10*, 222.
[21] N. von den Driesch, D. Stange, S. Wirths, D. Rainko, I. Povstugar, A. Savenko, U. Breuer, R. Geiger, H. Sigg, Z. Ikonic, J. Hartmann, D. Grützmacher, S. Mantl, D. Buca, *Small* **2017**, *13*, 1603321.
[22] N. von den Driesch, D. Stange, S. Wirths, G. Mussler, B. Holländer, Z. Ikonic, J. M. Hartmann, T. Stoica, S. Mantl, D. Grützmacher, D. Buca, *Chem. Mater.* **2015**, *27*, 4693.
[23] D. Spirito, N. von den Driesch, C. L. Manganelli, M. H. Zoellner, A. A. Corley-Wiciak, Z. Ikonic, T. Stoica, D. Grützmacher, D. Buca, G. Capellini, *ACS Appl. Energy Mater.* **2021**, *4*, 7385.
[24] C. L. Manganelli, M. Virgilio, O. Skibitzki, M. Salvalaglio, D. Spirito, P. Zaumseil, Y. Yamamoto, M. Montanari, W. M. Klesse, G. Capellini, *J. Raman Spectrosc.* **2020**, *51*, 989.
[25] A. Ghrib, M. El Kurdi, M. Prost, S. Sauvage, X. Checoury, G. Beaudoin, M. Chaigneau, R. Ossikovski, I. Sagnes, P. Boucaud, *Adv. Opt. Mater.* **2015**, *3*, 353.

© 2022 The Authors. Advanced Optical Materials published by Wiley-VCH GmbH

21951071, 2022, 22, Downloaded from https://onlinelibrary.wiley.com/doi/10.1002/adom.202201024 by Test, Wiley Online Library on [22/12/2022]. See the Terms and Conditions (https://onlinelibrary.wiley.com/terms-and-conditions) on Wiley Online Library for rules of use; OA articles are governed by the applicable Creative Commons License

[26] A. Elbaz, M. El Kurdi, A. Aassime, S. Sauvage, X. Checoury, I. Sagnes, F. Bøeuf, P. Boucaud, *Opt. Express* **2018**, *26*, 28376.
[27] V. Reboud, A. Gassenq, N. Pauc, J. Aubin, L. Milord, Q. M. Thai, M. Bertrand, K. Guilloy, D. Rouchon, J. Rothman, T. Zabel, F. Armand Pilon, H. Sigg, A. Chelnokov, J. M. Hartmann, V. Calvo, *Phys. Lett.* **2017**, *111*, 092101.
[28] W. Du, Q. M. Thai, J. Chrétien, M. Bertrand, L. Casiez, Y. Zhou, J. Margetis, N. Pauc, A. Chelnokov, V. Reboud, V. Calvo, J. Tolle, B. Li, S.-Q. Yu, *Front. Phys.* **2019**, *7*, 147.
[29] Q. M. Thai, N. Pauc, J. Aubin, M. Bertrand, J. Chrétien, V. Delaye, A. Chelnokov, J.-M. Hartmann, V. Reboud, V. Calvo, *Opt. Express* **2018**, *26*, 32500.
[30] S. Assali, M. Elsayed, J. Nicolas, M. O. Liedke, A. Wagner, M. Butterling, R. Krause-Rehberg, O. Moutanabbir, *Appl. Phys. Lett.* **2019**, *114*, 251907.
[31] L. Groell, A. Attiaoui, S. Assali, O. Moutanabbir, *J. Phys. Chem. C* **2021**, *125*, 9516.
[32] D. Rainko, Z. Ikonic, N. Vukmirović, D. Stange, N. von den Driesch, D. Grützmacher, D. Buca, *Sci. Rep.* **2018**, *8*, 15557.

© 2022 The Authors. Advanced Optical Materials published by Wiley-VCH GmbH

21951071, 2022, 22, Downloaded from https://onlinelibrary.wiley.com/doi/10.1002/adom.202201024 by Test, Wiley Online Library on [22/12/2022]. See the Terms and Conditions (https://onlinelibrary.wiley.com/terms-and-conditions) on Wiley Online Library for rules of use; OA articles are governed by the applicable Creative Commons License